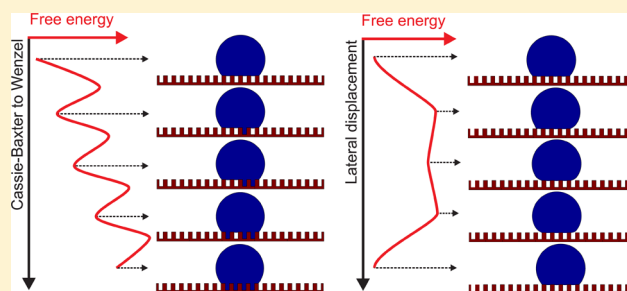


## Minimum Energy Paths of Wetting Transitions on Grooved Surfaces

George Pashos,<sup>\*,†</sup> George Kokkoris,<sup>†,‡</sup> and Andreas G. Boudouvis<sup>†</sup><sup>†</sup>School of Chemical Engineering, National Technical University of Athens, Zografou Campus, Athens 15780, Greece<sup>‡</sup>Institute of Nanoscience & Nanotechnology, NCSR Demokritos, Athens 15310, Greece

**ABSTRACT:** A method that computes minimum energy paths (MEPs) of wetting transitions is developed. The method couples the Cahn–Hilliard formulation of a modified phase-field method with the simplified string method. Its main computational kernel is the fast Fourier transform that is efficiently performed on graphics processing units. The effectiveness of the proposed method is demonstrated on two types of transitions of droplets on grooved surfaces. The first is the transition from the Cassie–Baxter wetting state to the Wenzel state, where it is shown that it progresses in a sequential manner with the droplet wetting each groove successively. The second transition type is a lateral displacement of the droplet against the grooves, where the droplet successively detaches/attaches from/to the rear/front protrusion of the surface (a transition in the reverse order is also possible). The energy barriers of both the transitions are extracted from the MEP; they are useful for the evaluation of the robustness of superhydrophobic surfaces (resistance to the Cassie–Baxter to Wenzel transition) and the droplet mobility on those surfaces (high mobility/small resistance to lateral displacements). The relation of the MEP with the potential transition paths coming from the solution space mapping is discussed.



## 1. INTRODUCTION

Superhydrophobic behavior of solid surfaces can be achieved by appropriately designing the surface morphology<sup>1,2</sup> (patterning) or imparting an artificial roughness that can span two or more length scales.<sup>2</sup> Patterned surfaces are characterized as superhydrophobic when droplets placed on them have high apparent contact angles and tend to slip easily (low hysteresis). The observed superhydrophobic state is referred to as the Cassie–Baxter (CB) wetting equilibrium state. It involves the droplet forming a composite three-phase interface (solid–liquid–air), with a small solid–liquid interface, i.e., the droplet sits on the protrusions of the patterned morphology, interacting with a small portion of the solid. However, the CB wetting state is often metastable and if perturbed, will transition to the Wenzel (W) wetting equilibrium state. The transition entails the collapse of the droplet into the morphology, maximizing the solid–liquid interface. The W state is accompanied by droplet pinning on abrupt geometric features and apparent contact angle reduction, which can be detrimental for applications that require robust superhydrophobic behavior. The design of patterned surfaces that resist the CB to W (CB–W) transitions can improve many applications such as self-cleaning surfaces,<sup>3,4</sup> microfluidic valves without mechanical parts,<sup>5</sup> etc.

The perturbation of the CB state may lead to different outcomes depending on its nature. For instance, if the perturbation is weak, the droplet–surface system will fail to transition to a different wetting state and will return to its original configuration. If the perturbation is strong but not properly “aimed”, then the system may reach the W state, but it would require an unnecessary surplus of energy. Depending on

the nature of the perturbation, each particular system responds differently, while displaying variable resistance—with respect to different perturbations—to the CB–W transition. Instead of focusing on the types of perturbations we seek the theoretically minimum disturbance required to initiate the transition. The minimum disturbance imparts enough energy to reach the energy saddle that connects two stable wetting states; the stable states are minima on the energy landscape of the system. Beyond the energy saddle, the system will spontaneously descend to the minimum that corresponds to the other equilibrium state. The minimum required energy to traverse an energy saddle is the energy barrier of the transition between two stable states. It can be used as a useful metric for the evaluation of the robustness of superhydrophobic surfaces.<sup>6–8</sup>

The transition path that connects two energy minima through an energy saddle is known in the literature as minimum energy path (MEP).<sup>9–13</sup> A MEP could contain multiple energy saddles, which means that there are equally as many stable equilibria between the saddles. This translates to droplet–surface systems with intermediate impregnating wetting states,<sup>14</sup> i.e., states that the droplet is partially submerged into the morphology. Moreover, there may be more than one MEP between two stable states,<sup>15</sup> indicating many energetically favorable wetting transitions. The MEP provides an interesting perspective of wetting phenomena with the computation of possible wetting transitions and the corresponding energy barriers.

Received: December 16, 2014

Revised: February 19, 2015

Published: February 25, 2015

In this work, we propose a method to compute the MEPs of wetting transitions that is specifically designed for fast computations and is able to efficiently harness the computational power of graphics processing units (GPUs). For the computations of MEPs, several methods have been developed, including the elastic band method,<sup>16</sup> the dimer method,<sup>17</sup> and the string method.<sup>15</sup> The latter approximates the MEP as a discretized curve that connects two minima on the energy landscape of the system. We use a simplified version of the string method<sup>18</sup> that has better convergence properties and smaller computational cost. The string method must be coupled with a method that computes wetting states, for which there are many possible approaches in the literature, ranging from molecular dynamics,<sup>7,19,20</sup> lattice Boltzmann,<sup>21–23</sup> level-set,<sup>24,25</sup> phase-field,<sup>26–29</sup> etc. Phase-field methods have already been successfully coupled with the simplified string method for problems of crystal formation<sup>30</sup> and wetting.<sup>31</sup> In ref 31, the MEPs of wetting transitions are computed through an Allen–Cahn (AC) formulation of phase-field, which requires an integral constraint for the conservation of the droplet volume. The computation of this integral on massively multithreaded environments significantly lowers the overall execution speed. Therefore, the alternative of the Cahn–Hilliard (CH) formulation<sup>32,33</sup> is considered, which innately conserves the droplet volume. However, the CH formulation is computationally more expensive than AC, in terms of operations per iteration, although the former has its own merits in terms of accuracy and convergence properties. The proposed framework of fast Fourier transform (FFT)-based computations tips the scales in favor of the CH formulation of a modified phase-field method.<sup>34</sup> It requires only an extra FFT per iteration (2 FFTs per iteration; see Appendix Step 4) compared to AC,<sup>35</sup> which proves to be executed faster than a single integration on a GPU. The utilized CH formulation includes the contribution of the solid phase without the requirement of an additional partial differential equation and in a manner that enables the efficient application of FFTs. The solution of the transformed system of discretized equations in the frequency domain circumvents the solution of large systems of equations and replaces them with simple arithmetic operations.

## 2. MATHEMATICAL FORMULATION

**2.1. Computation of Wetting States.** The wetting states are computed through the CH formulation of a modified phase-field method,<sup>34</sup> according to which the mixing energy of the system,<sup>36,37</sup> augmented with the contribution of the solid, is

$$f_{\text{mix}}(\varphi, \nabla \varphi) = \frac{1}{2} \lambda |\nabla \varphi|^2 + \frac{(1 + \alpha)}{2} \frac{\lambda}{4\epsilon^2} (\varphi^2 - 1)^2 + \frac{(1 - \alpha)}{2} \frac{\lambda}{2\epsilon^2} k_s (\varphi - \varphi_s)^2 \quad (1)$$

where  $\varphi$  denotes the phase-field, i.e., the spatial variable that indicates the distribution of the phases ( $\varphi = 1$  liquid,  $\varphi = -1$  air,  $\varphi = \varphi_s$  solid; see below). The parameter,  $\lambda$ , is the mixing energy density<sup>38,39</sup> that is related to the surface tension through  $\sigma = 2\sqrt{2}\lambda/3\epsilon$ , and  $\epsilon$  is the capillary width<sup>32,40</sup> that controls the thickness of the diffuse interface. The spatial parameter,  $\alpha$ , marks the solid phase in the following fashion:  $\alpha = -1$  if solid is present and  $\alpha = 1$ , otherwise. The first term on the right-hand side (RHS) of eq 1 corresponds to the interfacial energy. It contributes to eq 1 mainly at the diffuse interface, where there

is a steep gradient of  $\varphi$ . The second term corresponds to the bulk phase energy,<sup>33,41–43</sup> which is a double-well potential energy density function with two minima at 1 and  $-1$ . Essentially, it ensures the immiscibility of the fluids by driving  $\varphi$  toward 1 (liquid) or  $-1$  (air). This term contributes to eq 1, only at areas occupied by the fluids ( $\alpha = 1$ ) and similarly, the third term that corresponds to the energy of the solid, has a contribution at areas where  $\alpha = -1$ . The contribution of the solid to the energy density is realized through a single-well potential function,<sup>44</sup> with minimum at  $\varphi = \varphi_s$ , where  $\varphi_s$  is directly related to the wettability of the solid, as it will be shown below. The single-well potential contains an arbitrary coefficient,  $k_s$ , which is assigned a sufficiently large value to adequately enforce  $\varphi = \varphi_s$ , wherever solid is present; unnecessarily large values will negatively affect the stability of the numerical scheme. The parameter,  $\varphi_s$ , is a function of the wettability of the solid, i.e., Young's contact angle:

$$\theta_Y = 90^\circ(1 - \varphi_s) \quad (2)$$

The derivation of eq 2 is simple. If  $\varphi_s = -1$ , then the presence of the solid is equivalent to that of the air, yielding  $\theta_Y = 180^\circ$  and likewise, if  $\varphi_s = 1$ , then  $\theta_Y = 0^\circ$ . This extends to all the intermediate states following a linear relation.

The free energy of the system is the integral, defined on the computational domain,  $\Omega$ , of the augmented mixing energy:

$$E(\varphi) = \int_{\Omega} \left( \frac{1}{2} \lambda |\nabla \varphi|^2 + \frac{(1 + \alpha)}{2} \frac{\lambda}{4\epsilon^2} (\varphi^2 - 1)^2 + \frac{(1 - \alpha)}{2} \frac{\lambda}{2\epsilon^2} k_s (\varphi - \varphi_s)^2 \right) dV \quad (3)$$

The functional derivative of eq 3 yields the chemical potential:

$$G = \frac{\lambda}{\epsilon^2} \left( -\epsilon^2 \nabla^2 \varphi + \frac{(1 + \alpha)}{2} (\varphi^2 - 1) \varphi + \frac{(1 - \alpha)}{2} k_s (\varphi - \varphi_s) \right) \quad (4)$$

A discretization of eq 4, with good numerical stability, requires the semi-implicit treatment of the second term on the RHS. However, the inclusion of the  $(1 + \alpha)/2$  factor prohibits any implicit treatment of this particular term within the FFT framework. To elaborate, only linear terms can be treated implicitly, for which the application of FFT yields  $C\bar{\varphi}$ , where  $\bar{\varphi}$  is the transformed  $\varphi$  and  $C$  is a constant. Consider the term,  $(\varphi^2 - 1)\varphi$ . The linear component of this term ( $-\varphi$ ) can be treated implicitly, whereas the nonlinear component ( $\varphi^3$ ) cannot. In contrast, the multiplication by the  $(1 + \alpha)/2$  factor produces a purely nonlinear term, because  $\alpha$  is essentially another phase-field indicating the solid. Therefore, the factor is set equal to 1, yielding a modified version of eq 4. The modified eq 4 erroneously applies the double-well potential—associated with the bulk energy of the fluids—to areas of the solid phase as well. Consequently, the value of  $\varphi$ , attained at the solid becomes significantly inconsistent with the correct value dictated by eq 2. To mitigate this effect,  $\varphi_s$  is replaced in the modified eq 4 by  $\varphi'_s$ , with the latter being approximated by

$$\varphi'_s = \frac{(\varphi_s^2 - 1)\varphi_s + k_s \varphi_s}{k_s} \quad (5)$$

The replacement of  $\varphi_s$  by  $\varphi'_s$  in eq 4 counteracts the effect of the double-well potential of the fluids on the solid and thus,

rectifies the modified eq 4. The formulation of eq 5 is accomplished as follows: For  $\alpha = -1$  and therefore,  $\varphi = \varphi_s$ , the chemical potential is equal to the diffusive term of eq 4. If the diffusive term is neglected, then eq 5 can be derived from eq 4, by setting the  $(1 + \alpha)/2$  factor equal to 1 and replacing  $\varphi$  and  $\varphi_s$  with the target value of  $\varphi$  ( $\varphi_s$ ) and the adjusted parameter,  $\varphi_s'$ , respectively. Despite the omission of the diffusive term in eq 5, the results show high accuracy. The modified eq 4 reads:

$$G = \frac{\lambda}{\varepsilon^2} \left( -\varepsilon^2 \nabla^2 \varphi + \varphi^3 - \varphi + \frac{(1 - \alpha)}{2} k_s (\varphi - \varphi_s') \right) \quad (6)$$

According to the CH formulation, the evolution of  $\varphi$  is conservative and has the form of a continuity equation:<sup>44</sup>

$$\frac{\partial \varphi}{\partial t} = \nabla \cdot (\mu \nabla G) \quad (7)$$

where  $\mu$  is the mobility that for the purposes of this work is considered constant and set equal to 1. The selection of  $\mu$  is justified, because the dynamics of the system in the context of proposed method are irrelevant. Moreover, since eq 7 conserves  $\varphi$ , it follows naturally that the droplet volume is conserved as well. The temporal discretization of eq 7, in conjunction with eq 6, is accomplished via a semi-implicit scheme:<sup>45</sup>

$$\begin{aligned} \varphi^{(n+1)} + \Delta \tau \nabla^2 [(1 - c_1) \varphi^{(n+1)} + (1 - c_2) \varepsilon^2 \nabla^2 \varphi^{(n+1)}] \\ = \varphi^{(n)} + \Delta \tau \nabla^2 \left[ -c_1 \varphi^{(n)} - c_2 \varepsilon^2 \nabla^2 \varphi^{(n)} + (\varphi^{(n)})^3 \right. \\ \left. + \frac{(1 - \alpha)}{2} k_s (\varphi^{(n)} - \varphi_s') \right] \end{aligned} \quad (8)$$

where  $n$  is the time step counter and  $\Delta \tau = \lambda \Delta t / \varepsilon^2$  ( $\Delta t$  – time step). The choice of the coefficients  $c_1$ ,  $c_2$ ,  $k_s$ , determines the stability of the numerical scheme and we opted for  $c_1 = 4$ ,  $c_2 = 0$ ,  $k_s = 5$ . The choice of  $k_s = 5$  is sufficient to adequately enforce  $\varphi = \varphi_s$ , without affecting the stability of the scheme, as long as  $\varphi_s$  doesn't have extreme values (close to 1 or  $-1$ ). Hydrophobic materials exhibit moderate  $\theta_y$ , which translates to  $\varphi_s$ , practically no smaller than  $-0.5$ . Therefore, for cases of practical interest, the purely explicit treatment of the term that involves  $k_s$ , will not affect the stability of the scheme. Overall, throughout the computational experiments, the numerical scheme (eq 8) was unconditionally stable, i.e., arbitrarily large time steps will not lead to divergence.

**2.2. Minimum Energy Path Computation.** The MEP connects two stable equilibrium states—corresponding to energy minima—via a curve,  $\gamma$ , on the energy landscape of the system. The MEP is aligned with energy valleys leading up to energy saddles that correspond to unstable equilibrium states and represents the most probable path that the system will follow.<sup>46</sup> To approximate the MEP,  $\gamma$  is discretized into an  $M$ -node piecewise linear curve, with each node representing an image,  $(\varphi_i, i = 1, 2, \dots, M)$ . Each image is a spatial arrangement of  $\varphi$ , not necessarily corresponding to an equilibrium state, unless the image in question is located at a minimum or a saddle. The curve,  $\gamma$ , is evolved by applying the component of generalized thermodynamic force that is normal to  $\gamma$ ,<sup>30</sup>  $(\nabla^2 G)^\perp(\gamma)$ , on each of the images. In this manner,  $\gamma$  will converge to the MEP where by definition,  $(\nabla^2 G)^\perp(\gamma) = 0$ . To compute the normal component of  $\nabla^2 G$ , a projection operation onto the tangent vector of  $\gamma$ , is required for each time step.

This, however, adds a considerable computational load to the method. If instead,  $\gamma$  is evolved with  $\nabla^2 G$ , it will not converge to the MEP, because the images descend toward the energy minima, i.e., every image will converge to a stable equilibrium state. According to the simplified string method,  $\gamma$  can be evolved with  $\nabla^2 G$ , if a reparameterization of  $\gamma$  is performed for each time step; all the images are redistributed along  $\gamma$ . For this work, the images are redistributed equidistantly; the distance is defined as  $d_i = \|\varphi_{i+1} - \varphi_i\|_2$ ,  $i = 1, 2, \dots, M - 1$  and the MEP arc-length up to the  $j$ th image:  $s_j = \sum_{i=1}^j d_i$ .

The images of the string method are evolved according to eq 7, augmented with a generalized curvature term of  $\gamma$  that essentially adds tension to the string:

$$\begin{aligned} \frac{\partial \varphi_i}{\partial t} &= \nabla^2 [G_i + D_s (2\varphi_i - \varphi_{i-1} - \varphi_{i+1})], \\ i &= 2, \dots, M - 1 \end{aligned} \quad (9)$$

where  $D_s$  is the curvature coefficient. This is done to avoid any overlapping of  $\gamma$  on itself, which usually destabilizes the numerical scheme. However, the addition of tension on the string, will lead to the computation of a path,  $\gamma'$ , that is theoretically not identical to the MEP, e.g., the string tension may induce some “corner-cutting” effects wherever the MEP turns abruptly. The curvature term (second term, RHS of eq 9) may be interpreted as an artificial stabilizing term and therefore, it is applied judiciously. Practically, the impact of the curvature term is kept as low as possible, while enabling convergence, by tuning  $D_s$ . The first and last images are stable equilibrium states that are computed and selected at an earlier stage—through eq 8—and thus, do not participate dynamically in the evolution of the string, i.e.,  $\varphi_1$  and  $\varphi_M$  are fixed.

The temporal discretization of eq 9 is done in a similar fashion to that of eq 7, yielding:

$$\begin{aligned} \varphi_i^{(n+1)} + \Delta \tau \nabla^2 [-3\varphi_i^{(n+1)} + \varepsilon^2 \nabla^2 \varphi_i^{(n+1)} - 2D_s \varphi_i^{(n+1)}] \\ = \varphi_i^{(n)} + \Delta \tau \nabla^2 \left[ -4\varphi_i^{(n)} + (\varphi_i^{(n)})^3 + \frac{(1 - \alpha)}{2} 5 \right. \\ \left. (\varphi_i^{(n)} - \varphi_s') - D_s (\varphi_{i-1}^{(n)} + \varphi_{i+1}^{(n)}) \right] \end{aligned} \quad (10)$$

where the curvature term is divided among the implicit and explicit parts of eq 10; the coefficients  $c_1$ ,  $c_2$ , and  $k_s$  are replaced by the selected values, 4, 0, and 5, respectively.

The spatial discretization of eq 10 can be achieved through any available method, e.g., finite differences, finite elements, etc., but usually involves the solution of a large linear system. Here instead, the spatial domain,  $\Omega$ —where  $\varphi$  is defined—is chosen to be rectangular, in order to transform eq 10 to the frequency domain<sup>47</sup> by means of the FFT. The transformation reduces eq 10 into a set of simple linear algebraic equations that are readily solved. To elaborate, initially  $\Omega$  is tessellated into a  $N$ -node uniform rectangular mesh. Therefore, each image,  $\varphi_i$ , has  $N$  degrees of freedom (DOFs),  $(\varphi_i(\mathbf{x}_j), i = 1, 2, \dots, M; j = 1, 2, \dots, N)$ , where  $\mathbf{x}$  is the spatial variable. The transformation of  $\varphi_i(\mathbf{x}_j)$  reads  $\bar{\varphi}_i(\mathbf{k}_j)$ , where  $\mathbf{k}$  is the wavenumber of the Fourier transform. Similarly, the transformed gradient operator is a simple multiplication operator,  $i\mathbf{k}$ , resulting in  $\nabla^2 \rightarrow -k^2, \nabla^4 \rightarrow k^4, k = |\mathbf{k}|$  according to which eq 10 is transformed to



$$\begin{aligned}
& (1 + 3\Delta\tau k^2 + \Delta\tau k^4 \varepsilon^2 + 2\Delta\tau k^2 D_s) \overline{\varphi_i^{(n+1)}} = \\
& (1 + 4\Delta\tau k^2) \overline{\varphi_i^{(n)}} - \Delta\tau k^2 (\overline{\varphi_i^{(n)}})^3 - \\
& \frac{5}{2} \Delta\tau k^2 (1 - \alpha) (\overline{\varphi_i^{(n)}} - \overline{\varphi_s^{(n)}}) + \Delta\tau k^2 D_s (\overline{\varphi_{i-1}^{(n)}} + \overline{\varphi_{i+1}^{(n)}})
\end{aligned} \quad (11)$$

Equation 11 is the basic computational kernel of the proposed method that can be solved directly for  $\overline{\varphi_i^{(n+1)}}$ . It encompasses the following operations in order of execution, per time step  $(n)$ , per image  $(i)$ :

- The FFTs,  $\varphi_i^{(n)} \rightarrow \overline{\varphi_i^{(n)}}$ ,  $(\varphi_i^{(n)})^3 \rightarrow (\overline{\varphi_i^{(n)}})^3$ ,  $(1-\alpha)(\varphi_i^{(n)} - \varphi_s^{(n)}) \rightarrow (1-\alpha)(\overline{\varphi_i^{(n)}} - \overline{\varphi_s^{(n)}})$ ,
- the solution of eq 11,
- the inverse FFT,  $\overline{\varphi_i^{(n+1)}} \rightarrow \varphi_i^{(n+1)}$ ,
- the computation of the distance,  $d_i^{(n+1)} = \|\varphi_{i+1}^{(n+1)} - \varphi_i^{(n+1)}\|_2$  and the redistribution of  $\varphi_i^{(n+1)}$  on the curve  $\gamma^{(n+1)}$ , which is essentially a linear interpolation on  $\gamma^{(n+1)}$  (piecewise linear curve in the  $N$ -dimensional space) using the constraint of equidistant images.<sup>30</sup>

The computational complexity of the method is dictated by the FFTs that is  $O(N \log N)$  and has the advantage of scaling almost linearly with the DOFs per image ( $N$ ) and linearly with the number of images ( $M$ ). The method can be applied to both 2-D and 3-D problems, using the same formulation that was presented. The mesh resolution for 3-D problems can be modest, with a practical number of elements per spatial dimension in the range of hundreds (e.g.,  $400^3$  elements per image). The solution of 3-D problems prompts the utilization of significant computational resources (clusters of GPUs). On the other hand, for 2-D problems, we are able to use very fine meshes with thousands of elements per spatial dimension (e.g.,  $5000^2$  elements per image), utilizing little computational resources. In this work, we tackle a 2-D problem with a mesh size of  $1024^2$  (see Section 3.1); the computations are performed on a single GPU (Tesla M2050).

### 3. RESULTS

#### 3.1. Wetting Transitions on Grooved Surfaces.

Consider a grooved surface with equally spaced rectangular grooves (Figure 1). On the top of the surface protrusions rests

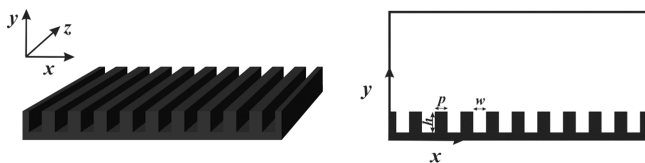


**Figure 1.** Patterned surface with uniform rectangular grooves. The wetting problem can be reduced to a 2-D computational problem on an  $x$ - $y$  cross-section;  $h = 0.041$ ,  $p = w = 0.0244$ .

a single droplet that is elongated in the direction of the grooves. The elongation of the droplet is commonly observed in systems of droplets on patterned surfaces with translational symmetry, e.g., grooved surfaces,<sup>48–51</sup> chemically striped patterned surfaces.<sup>52,53</sup> Neglecting the effects on the edges of the symmetry axis ( $z$ -axis), the computational problem can be reduced to a 2-D problem on an  $x$ - $y$  cross-section. The 2-D

computational domain,  $\Omega = [1,1]$ , is tessellated into  $1024 \times 1024$  square elements ( $N = 1\,048\,576$  DOFs per image), and the MEP is discretized into  $M = 40$  images, for a total of  $M \times N = 41\,943\,040$  DOFs. The first and last images are computed only once, since they are fixed throughout the convergence process of the string method and thus, the effective DOFs are  $(M - 2) \times N = 39\,845\,888$ . The chosen parameter values are  $\varepsilon = 0.0016$ ,  $D_s = 0.03$ ,  $\varphi_s = -0.25$  ( $\theta_Y = 112.5^\circ$  – slightly greater than Young's angle of water on Teflon films) and the frequency of application of the reparameterization step,  $n' = 50$  (see Appendix).

The selection for the first image is a stable equilibrium CB wetting state, with the droplet on top of five protrusions of the surface (Figure 2A(i)) and for the last image is a stable W

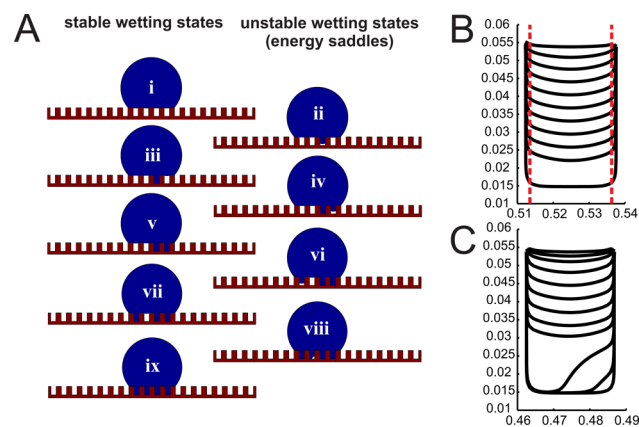


**Figure 2.** (A) MEP images (energy minima and saddles) of the CB (i) to W (ix) transition of a droplet on a grooved surface. (B) Detailed view, inside the groove, of the MEP images connecting (i) and (iii). The segments of the menisci between the dashed lines are used to derive the advancing contact angle through a circular fitting. The other symmetric transitions: (iii)–(v) and (v)–(vii) are virtually identical to (i)–(iii). (C) Detailed view of the asymmetric transition (vii)–(ix).

wetting state, with the droplet wetting the four grooves between the outer protrusions (Figure 2A(ix)). According to the computed MEP, the droplet reaches the W state by wetting each groove successively, crossing three intermediate stable impregnating states (Figure 2A(iii),(v),(vii)) before reaching the W state. The sequence in which the grooves are wetted is 2-1-4-3 (from right to left) and largely depends on the initial estimation of the MEP. Other MEPs have been computed as well, with different wetting sequences such as 1-2-4-3, 3-4-1-2, and 4-3-1-2, the last two being the mirror images of the first two. This reveals a multiplicity of MEPs for this particular system, with negligible differences in the energy barriers. We can speculate that the method is unbiased regarding the wetting sequence of the grooves, thus expecting 24 virtually equivalent (in terms of energy barriers) MEPs.

The sequential manner of CB–W transitions on grooved surfaces differs fundamentally from the transitions on pillared surfaces. The formed menisci are isolated from each other, since they are confined between the edges of each groove. In contrast, a single composite meniscus is formed on pillared surfaces. To illustrate the difference, a localized sagging of the meniscus will affect adjacent areas, pulling the droplet toward a W state,<sup>54</sup> whereas for grooved surfaces, a localized sagging could lead to a wetting transition only for the corresponding groove. In ref 54, the meniscus of a droplet on a pillared surface

is visualized, based on experimental results. It is shown that the depinning of the droplet at an arbitrary location will lead to a spontaneous transition to the W state. In other terms, it is equivalent to say that the system traverses a single energy saddle during the transition. Computations of CB-W MEPs agree to the aforementioned experimental observations and were presented in ref 31. It was shown that the system of a droplet on a  $5 \times 5$  square pillar array traverses only a single energy saddle. In this work, it is shown that the system of a droplet on a grooved surface must traverse as many energy saddles (Figure 2A(ii),(iv),(vi),(viii)) as the number of grooves.

The MEP of the wetting transition for each groove can be separated into the following segments (Figure 2B): Initially, the curvature of the meniscus increases, while the liquid is still pinned on the edges of the groove. Depinning is predicted according to the Gibbs criterion,<sup>55,56</sup> i.e., for this case of smooth rectangular grooves when the advancing contact angle surpasses  $\theta_Y$ . We compute the advancing contact angle by fitting a circular segment to the zero iso-contour of  $\phi$ . The iso-contour is cutoff near the solid walls at a distance of 0.0013 (dimensionless), in order to level the effect of the diffuse interface near the walls; the cutoff length is as small as possible, while providing an acceptable fitting. The advancing contact angle was computed at  $113.2^\circ$  ( $\theta_Y = 112.5^\circ$ ). After the depinning, the meniscus maintains constant curvature during a symmetric descent toward the bottom of the groove. Finally, the groove becomes fully wetted when the system traverses an energy saddle. The energy saddle corresponds to the MEP image, where only a small air pocket remains<sup>57</sup> (Figure 2A(ii),(iv),(vi)). The existence of an energy saddle, marginally close to the full wetting state inside a groove, was predicted in ref 57. This was performed by the minimization of the free energy using simplified calculations. In ref 48, a simplified formula was employed to calculate the critical impact velocity of a droplet that leads to the full wetting of a single groove. The introduced formula can be also used to predict the critical pressure that initiates the wetting transition inside a groove. Given the dimensions of the grooves (Figure 1), the critical pressure is calculated through the simplified formula:  $P_{\text{crit}} = 2\sigma \sin^4(\theta_Y/2)/w$  at 2820 Pa;  $\sigma = 72$  mN/m and groove dimensions in millimeters. The critical pressure, through the proposed method, is calculated at 2460 Pa. The calculation is accomplished by estimating the radius of curvature ( $1/R$ ) of the descending meniscus (Figure 2B), which yields the critical pressure through  $P_{\text{crit}} = \sigma/R$ .

The computed wetting transition for the third groove from the right is asymmetric (Figure 2C).<sup>58</sup> The meniscus descends symmetrically (identical to the transition of the other grooves) until a certain point where the symmetry breaks and a sidewall is entirely wetted, while the other is not. In ref 58, this was interpreted using geometric terms: below a certain height, a meniscus that is confined between the bottom and a sidewall has smaller surface area and therefore, lower free energy than a meniscus between the sidewalls. The computed type of transition (symmetric or asymmetric) depends on the initial estimation of the MEP. All possible sequences involving both these types are essentially MEPs, with only marginal differences regarding practically useful quantities, e.g. energy barriers.

The energy saddles (Figure 2A(ii),(iv),(vi),(viii)) of the MEP that connect two wetting states, must be surpassed in order to enable the wetting transition, e.g., to switch from state (iii) to (vii), both energy saddles (iv) and (vi) are surpassed, etc. The energy barriers of these transitions can be conveniently

deduced from the free energy plot of the MEP (Figure 3), where the peaks correspond to the energy saddles and the

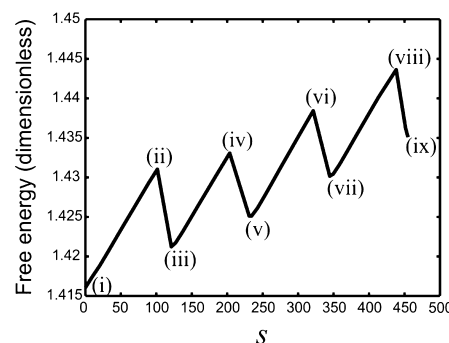


**Figure 3.** Free energy of the CB (i) to W (ix) MEP of a droplet on a grooved surface versus its arc-length. The marked images of the MEP correspond to equilibrium wetting states (energy minima and saddles) and are drawn in Figure 2A.

troughs to the stable wetting states. The free energy is plotted against the MEP arc-length that represents the progress of the transition. It is also plotted in dimensionless form, using the reference energy  $\sigma\Omega^2$ , where  $\sigma$  is the surface tension of the liquid and  $\Omega^2$  is the surface area of the computational domain. The energy barriers are defined as the energy difference of peaks from adjacent troughs, e.g., to compute the energy barrier of the transition from CB (i) to the first impregnating state (iii), the energy of (i) is subtracted from the energy of the first energy saddle (ii):  $E_{i \rightarrow iii} = E_{ii} - E_i$ ; similarly for the backward transition:  $E_{iii \rightarrow i} = E_{ii} - E_{iii}$ . If the system traverses several energy saddles, then the energy barrier of the overall transition is computed as the sum of the individual energy barriers of the trough-to-trough segmented MEP, e.g., the energy barrier of the CB–W transition is  $E_{i \rightarrow ix} = (E_{ii} - E_i) + (E_{iv} - E_{iii}) + (E_{vi} - E_v) + (E_{viii} - E_{vii})$ . The CB–W energy barrier is the minimum required energy for a quasi-static transition, which implies energy dissipation when the system traverses descending segments of the MEP. In contrast, if the system conserves energy, then, during descending segments, the droplet will gather momentum, and inertial effects will take place. Theoretically, the accumulated energy may be adequate to surpass the subsequent energy barriers. Then the required energy of the CB–W transition is equal to the largest individual energy barrier. In this case, however, if the inertial effects are uncontrollable, the system may be driven to unpredicted wetting states.

The proposed method can evaluate the mobility of the droplet on a grooved surface by computing the MEP of a lateral displacement of the droplet. High energy barriers of the lateral transition suggest low mobility of the droplet, whereas low energy barriers suggest high mobility, encompassing low hysteresis, easy droplet roll-off, etc. The MEP of the lateral displacement shows that the droplet skips a groove by initially detaching from the rear protrusion and then attaching on the protrusion at the moving front (Figure 4, column D); this particular droplet–grooves system is identical to the previous (Figure 2A). The droplet detachment and attachment correspond to energy saddles; a high-energy stable wetting state exists between them with the droplet on top of four protrusions, instead of five at the initial wetting state. The MEP is periodic in the direction of the lateral displacement and has the characteristic length equal to the geometric periodicity of

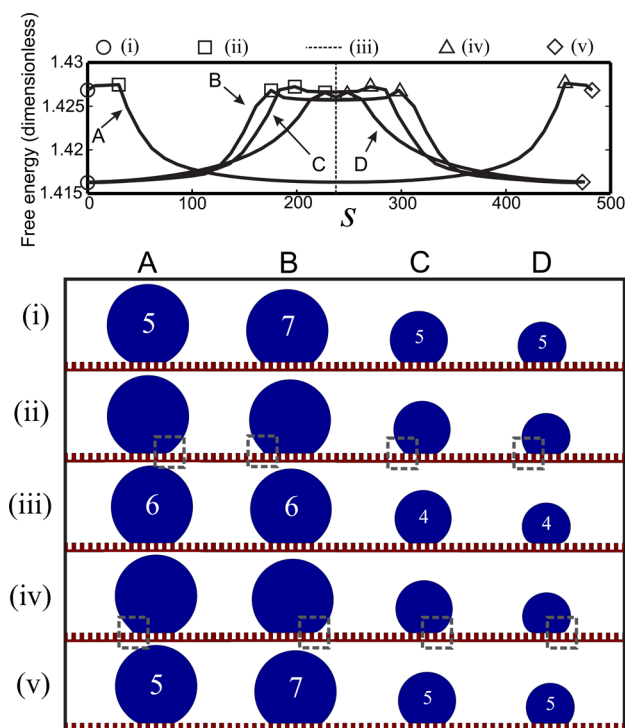


**Figure 4.** Free energies of lateral transition MEPs (A, B, C, D) versus their arc-length. Selected MEP images (energy minima and saddles) that are marked on the diagram are drawn below. Each column represents a droplet–grooves system, and each row represents a wetting state; (i), (iii), and (v) energy minima, (ii) and (iv) energy saddles. The dashed line boxes indicate the location of the attachment/detachment. The number of protrusions underneath each droplet is shown as well (column A: 5–6–5, etc.). During the transitions the droplet skips a single groove, by either detaching/attaching from the rear/front protrusion (B, C, D) or vice versa (A). The droplet volumes are 0.193, 0.185, 0.0925, and 0.0624 for A, B, C, and D, respectively (dimensionless). The free energies of A, B, and C are adjusted accordingly to match the baseline energy of D, in order to facilitate the comparison of the energy barriers; the MEP arc-length is adjusted as well. The cross-section of the intermediate stable wetting state D-(iii) deviates slightly from a perfectly circular bulk profile due to the coarse approximation of the energy minimum between two energy saddles (D-(ii) and (iv)) that are in very close proximity.

the grooved surface. Thus, the method yields a single energy barrier per skipped groove equal to  $E_{i \rightarrow v} = (E_{ii} - E_i) + (E_{iv} - E_{iii})$  (Figure 4).

Systems with larger droplets show identical lateral displacement MEPs (in terms of energy barriers) with only negligible discrepancies, mainly attributed to the numerical approximation. The examined systems include four droplet–pillar systems with increasing droplet volume; initial/final MEP images have the droplet on five protrusions. Also, another system is presented, where the initial/final MEP images have the droplet on seven protrusions. The transition for all examined systems initiates with the detachment from the rear protrusion and concludes with the attachment to the front. The exception is the system with the largest droplet volume, where the transition occurs in reverse order (attachment/detachment) (Figure 4, column A). Otherwise, the droplet would have to attain a stable state on four pillars that is impossible given the large volume of the droplet. Similar experimental observations, although for pillared surfaces, can be found in the Supporting Information of ref 54, where it is evident that the droplet initially detaches

from the rear pillar and then attaches to the front. The free energies of the examined systems are presented in Figure 4, offset by a constant value to match the baseline of the lowest energy MEP (for demonstration purposes). The energy barriers for all cases are almost equal, which suggests equal mobility regardless the droplet volume or the area of the liquid–solid interface (five or seven protrusions). The invariance of the energy barriers is attributed to the primarily local effect of the MEP generalized force that acts in a small region at the rear and front protrusion. Therefore, neither the bulk of the droplet nor the size of liquid–solid interface area noticeably affects the transition and consequently the energy barriers. Moreover, the advancing/receding contact angles, computed for the MEP images that correspond to energy saddles, are invariant as well. The advancing/receding contact angles are derived from the slope of the zero isocontour of  $\varphi$  at a vertical distance of 0.0013 (cf. above advancing contact angle in a groove) from the top of the protrusions. The receding contact angle is estimated at  $\sim 116^\circ$ , across all examined systems, when they reach the energy saddle corresponding to the droplet detachment. Similarly, the advancing contact angle is estimated at  $\sim 163^\circ$  when the systems reach the energy saddle corresponding to the droplet attachment; the aforementioned contact angles are computed for two different wetting states (Figure 4, rows (ii) and (iv)). This suggests that, despite changes in the droplet volume or the liquid–solid interface area, the local forces at the rear/front three-phase contact line are invariant and, by extension, so is the MEP driving force. The chosen parameter values for the lateral displacement MEP are  $\varepsilon = 0.0016$ ,  $D_s = 0.03$ ,  $\varphi_s = -0.25$  ( $\theta_Y = 112.5^\circ$ ) and  $n' = 20$ .

**3.2. Comparison with Potential Transition Paths from the Mapping of the Solution Space.** The MEP can be deduced from a comprehensive mapping of the solution space of the droplet–surface system. However, as the complexity of the surface morphology increases, the complexity of the solution space increases as well. The solution space exhibits often a vast number of solution branches, so that the bifurcation diagram becomes very impractical or in the best case, open to interpretation.<sup>34</sup> For the purposes of this work, we present a simple bifurcation diagram of a droplet–surface system that suggests two candidates for the MEP as it will be shown below.

The droplet–surface system consists of a droplet on two rectangular protrusions with translational symmetry, and its solution space is mapped by a parameter continuation technique<sup>59</sup> with respect to the parameter,  $\theta_Y$ , coupled with a steady-state solver based on eq 4.<sup>34</sup> For this problem, the computational domain,  $\Omega = [1, 1]$ , is tessellated into  $150 \times 150$  square elements ( $N = 22\,500$  DOFs), and the protrusions are of the same design as those of Figure 1. The reduction of DOFs is required in order to have the mapping of the solution space within a sensible time frame. The MEP is discretized into  $M = 80$  images, with  $\varepsilon = 0.01$ ,  $D_s = 0.001$  and  $\varphi_s = -0.25$  ( $\theta_Y = 112.5^\circ$ ).

The system has two types of solution families: one that has only symmetric solutions (black S-curve, Figure 5), and one that has asymmetric solutions (blue S-curve, Figure 5). For  $\theta_Y = 112.5^\circ$ , six wetting states are encountered: three that correspond to symmetric states, denoted (A), (B), and (C), and three that correspond to asymmetric states, denoted (a), (b), and (c). The asymmetric solutions have mirror-image counterparts, which are exactly equivalent to the original solutions and therefore not shown. The (A) and (C) states are



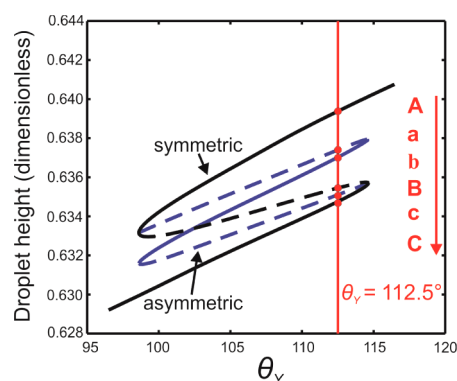


**Figure 5.** Bifurcation diagram of the system of a droplet on two rectangular protrusions (droplet height versus contact angle). The droplet height is dimensionless with reference to the height of the computational domain,  $\Omega = [1,1]$ . Black line: family of symmetric solutions. Blue line: family of asymmetric solutions. Solid line segments: stable wetting states branch. Dashed line segments: unstable wetting states branch. The marked (with dots) solutions are in order of appearance from top to bottom: (A), (a), (b), (B), (c), (C). The symmetric/asymmetric solutions are denoted by uppercase/lowercase letters and are drawn in Figure 6.

the CB and W, respectively, while (B) belongs to the branch of symmetric unstable states, where the droplet partially wets both the grooves. The (b) state is an intermediate impregnating wetting state, with the droplet wetting a single groove. The (a) and (c) states are unstable, with the droplet partially wetting a single groove ((a) state) or partially wetting a single groove while fully wetting the other ((c) state). All the aforementioned wetting states are gathered in Figure 6 (left part).

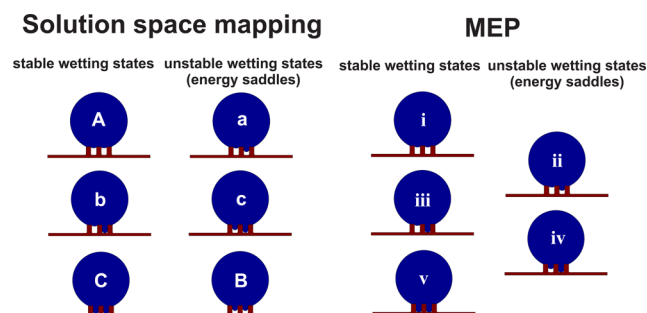


**Figure 6.** Various wetting states of a droplet on two rectangular protrusions for  $\theta_y = 112.5^\circ$ . On the left, the wetting states are obtained through the mapping of the solution space (Figure 5), whereas for the wetting states on the right, the proposed method is used. The sequence in which the wetting states are attained (not necessarily the entirety of those depicted) during a CB–W transition is discernible only via the proposed method (MEP) and only speculative otherwise (solution space mapping). Due to the large  $\varepsilon$  that was used (for the purposes of the comparison), which effectively “smears” the sharp droplet profile, the drawn isocontour erroneously implies a barely visible air pocket between droplet and groove for the wetting states (b), (C), (c), (iii), (iv), and (v).

Two candidates for the MEP emerge from the mapping of the solution space. The first candidate is symmetric, where the system makes a transition from (A) directly to (C) by traversing the energy saddle (B). The second is asymmetric, where the system attains the intermediate impregnating state (b) starting from (A) and traversing the energy saddle (a). The system finally reaches (C) from (b) through the energy saddle

(c). The solution space mapping, however, does not indicate which transition is preferable and therefore it is not possible to deduce the MEP solely by it. The proposed method reveals that the MEP is in fact asymmetric (Figure 6, right part) and its energy plot is shown in Figure 7. The MEP was computed for

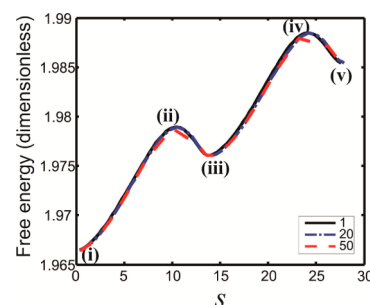


**Figure 7.** Free energy of the CB (i) to W (v) MEP of a droplet on two rectangular protrusions versus its arc-length. The marked images of the MEP correspond to wetting states (energy minima and saddles) and are drawn in Figure 6. The various lines correspond to different values of  $n'$  (frequency of application of the reparameterization step); black line:  $n' = 1$ , blue line:  $n' = 20$ , red line:  $n' = 50$ .

various values of  $n'$ , where it can be seen that even for  $n' = 50$  the MEP is quite well approximated, despite the coarsening of the MEP images near the energy saddles.

#### 4. CONCLUDING REMARKS

A MEP computation method was successfully coupled with the CH formulation of a modified phase-field method. The special formulation of the phase-field method allows the solution of the discretized partial differential equation in the frequency domain through the use of FFTs and enables fast computations on GPUs. The proposed method has been applied to droplet–surface systems with translational symmetry (a droplet on a grooved surface) for the MEP computation of CB–W transitions and droplet lateral displacements.

The MEP provides an absolute reference for any wetting transition because it is not necessary to include an actuation force, such as pressure, gravity, electric field, etc., to commence the transition. The energy barriers can be readily computed through the free energy of the computed MEP, which can be used to evaluate the robustness of a superhydrophobic surface. The CB–W transition for droplets on grooved surfaces is asymmetric in the sense that the grooves are wetted successively, with no persistent preference in the specific order. High CB–W energy barriers indicate robust superhydrophobic surfaces, however, the high resistance to the CB–W transition may have an adverse effect on the mobility of the droplets. Therefore, the MEP of a lateral transition of the droplet is computed in tandem with the CB–W MEP, which can be used to evaluate the resistance to lateral droplet displacements. The lateral transition MEP initiates with the droplet detaching from the rear protrusion, then attains a CB state and attaches to the protrusion in the direction of propagation. The lateral transition may also proceed in reverse order (attachment/detachment), depending on the droplet volume. Low energy barriers of lateral transitions indicate high droplet mobility and low hysteresis. The CB–W and lateral transition MEPs together provide a more broad evaluation of the wetting properties of patterned surfaces.

## ■ APPENDIX: COMPUTATIONAL IMPLEMENTATION

The presented method is intended for execution on GPUs, where the arithmetic operations in (11), the FFTs, the inverse FFT and the interpolation, tap well into the computational power of the GPUs. However, the operational model of the GPUs for computations, relies on the massively multithreaded execution, which unfortunately does not work well for reduction operations, such as dot products, norms, etc., and in this case the computation of the distance between images,  $d_i^{(n+1)} = \|\varphi_{i+1}^{(n+1)} - \varphi_i^{(n+1)}\|_2$ . As a result, the distance computation step slows down the execution of the whole process significantly.

The slowdown of the solution process can be remedied by simply requiring the reparameterization step and therefore, the distance computation step, to be applied periodically every  $n'$  time steps, instead of every time step. The execution time savings are substantial, and the accuracy of the predicted MEP is not affected considerably if a sensible  $n'$  is selected; in this work,  $n'$  ranges between 1 and 50. The algorithmic details of the proposed method are summarized in the following steps:

Step 1: The first and last images,  $\varphi_1$  and  $\varphi_M$ , are computed via eq 8, correspond to stable equilibrium states, and are fixed throughout the following steps.

Step 2: The initial estimates of the intermediate images are computed by a simple linear interpolation,  $(\varphi_i^{(1)}, i = 2, \dots, M - 1)$ , as equidistant points on the  $N$ -dimensional straight line that connects  $\varphi_1$  and  $\varphi_M$ .

Step 3: Compute for every intermediate image the FFT,  $\varphi_i^{(1)} \rightarrow \overline{\varphi_i^{(1)}}$ ,  $i = 2, \dots, M - 1$ .

Step 4: Initialize the time step counter,  $n = 1$ . Compute for every intermediate image ( $i = 2, \dots, M - 1$ ) the FFTs,  $(\varphi_i^{(n)})^3 \rightarrow \overline{(\varphi_i^{(n)})^3}$ ,  $(1 - \alpha)(\varphi_i^{(n)} - \varphi_s') \rightarrow (1 - \alpha)(\overline{\varphi_i^{(n)}} - \overline{\varphi_s'})$ . Derive  $\varphi_i^{(n+1)}$  from

$$\begin{aligned} & (1 + 3\Delta\tau k^2 + \Delta\tau k^4 \varepsilon^2 + 2\Delta\tau k^2 D_s) \overline{\varphi_i^{(n+1)}} = \\ & (1 + 4\Delta\tau k^2) \overline{\varphi_i^{(n)}} - \Delta\tau k^2 \overline{(\varphi_i^{(n)})^3} - \\ & \frac{5}{2} \Delta\tau k^2 (1 - \alpha) (\overline{\varphi_i^{(n)}} - \overline{\varphi_s'}) + \Delta\tau k^2 D_s (\overline{\varphi_{i-1}^{(1)}} + \overline{\varphi_{i+1}^{(1)}}). \end{aligned}$$

Compute the inverse FFT,  $\overline{\varphi_i^{(n+1)}} \rightarrow \varphi_i^{(n+1)}$ . Assign  $\overline{\varphi_i^{(n)}} \leftarrow \overline{\varphi_i^{(n+1)}}$ ,  $n \leftarrow n + 1$  and iterate Step 4 until  $n = n'$ .

Notice that the explicit part of the curvature term is approximated as constant throughout the iterations of Step 4, which reduces the overall FFTs –  $\varphi_i^{(n)} \rightarrow \overline{\varphi_i^{(n)}}$  not required during Step 4, and allows independent computations for each image; the solution for the image,  $\varphi_i^{(n+1)}$ , does not require information from the adjacent images,  $\varphi_{i-1}^{(n)}$  and  $\varphi_{i+1}^{(n)}$ . This practically permits the evolution of the images in a serial fashion from  $i = 2$  to  $i = M - 1$ , i.e., each image is evolved for  $n'$  time steps, before processing the next image, rather than evolving the whole string of images for a single time step and reiterating afterward.

Step 5: Compute the distance between images,  $d_i = \|\varphi_{i+1}^{(n')} - \varphi_i^{(n')}\|_2$ ,  $i = 1, \dots, M - 1$ .

Step 6: Compute the linearly interpolated images,  $\varphi_i^*$ , using the equidistant constraint. For the first iteration of Step 6, compute the initial error:  $e_{\text{init}} = \sum_{i=1}^M \|\varphi_i^{(1)} - \varphi_i^*\|$ . The convergence criterion for this work is the relative error defined

as  $e = \sum_{i=1}^M \|\varphi_i^{(1)} - \varphi_i^*\| / e_{\text{init}}$  with tolerance  $10^{-5}$ . If the convergence criterion is satisfied, terminate. Otherwise, assign  $\varphi_i^{(1)} \leftarrow \varphi_i^*$  and repeat the process from Step 3.

Steps 1–6 are executed serially, although Steps 4 and 5 can be executed simultaneously, in the following manner: In Step 4 each image is evolved all the way through to the  $n'$ th time step, and then the algorithm proceeds to the next image. For example, let  $\varphi_2^{(n')}$  be the completed image and  $\varphi_3^{(n')}$  be the working image. Then  $d_1 = \|\varphi_2^{(n')} - \varphi_1^{(n')}\|_2$  can be computed by a separate set of GPU threads, simultaneously with the computation of  $\varphi_3^{(n')}$  and so forth. The simultaneous execution of Steps 4 and 5 will “mask” the inefficiency of Step 5 and could allow for lower values of  $n'$ , while utilizing the full computational power of the GPUs.

## ■ AUTHOR INFORMATION

### Corresponding Author

\*E-mail: gpashos@chemeng.ntua.gr.

### Notes

The authors declare no competing financial interest.

## ■ ACKNOWLEDGMENTS

This work was cofinanced by Hellenic Funds and by the European Regional Development Fund (ERDF) under the Hellenic National Strategic Reference Framework (NSRF) 2007–2013, of the Project “THALES – DESIREDROP: DESIGN and fabrication of Robust superhydrophobic/philic surfaces and their application in the realization of “smart” microfluidic valves” (Contract No. MIS 380835). The authors would like to thank the reviewers for their insightful comments that led to some interesting findings.

## ■ ABBREVIATIONS

MEP, minimum energy path; FFT, fast Fourier transform; CB, Cassie–Baxter; W, Wenzel; CH, Cahn–Hilliard; AC, Allen–Cahn; DOFs, degrees of freedom; GPU, graphics processing unit

## ■ REFERENCES

- (1) Gnanappa, A. K.; Papageorgiou, D. P.; Gogolides, E.; Tserepi, A.; Papathanasiou, A. G.; Boudouvis, A. G. Hierarchical, Plasma Nanotextured, Robust Superamphiphobic Polymeric Surfaces Structurally Stabilized Through a Wetting–Drying Cycle. *Plasma Processes Polym.* **2012**, *9*, 304–315.
- (2) Ellinas, K.; Tserepi, A.; Gogolides, E. From Superamphiphobic to Amphiphilic Polymeric Surfaces with Ordered Hierarchical Roughness Fabricated with Colloidal Lithography and Plasma Nanotexturing. *Langmuir* **2011**, *27*, 3960–3969.
- (3) Verho, T.; Korhonen, J. T.; Sainiemi, L.; Jokinen, V.; Bower, C.; Franze, K.; Franssila, S.; Andrew, P.; Ikkala, O.; Ras, R. H. A. Reversible Switching between Superhydrophobic States on a Hierarchically Structured Surface. *Proc. Natl. Acad. Sci. U.S.A.* **2012**, *109*, 10210–10213.
- (4) Ellinas, K.; Tserepi, A.; Gogolides, E. Superhydrophobic, Passive Microvalves with Controllable Opening Threshold: Exploiting Plasma Nanotextured Microfluidics for a Programmable Flow Switchboard. *Microfluid. Nanofluid.* **2014**, *1*–10.
- (5) Tsougeni, K.; Papageorgiou, D.; Tserepi, A.; Gogolides, E. “Smart” Polymeric Microfluidics Fabricated by Plasma Processing: Controlled Wetting, Capillary Filling and Hydrophobic Valving. *Lab Chip* **2010**, *10*, 462–469.
- (6) David, R.; Neumann, A. W. Energy Barriers between the Cassie and Wenzel States on Random, Superhydrophobic Surfaces. *Colloids Surf. A: Physicochem. Eng. Aspects* **2013**, *425*, 51–58.



- (7) Savoy, E. S.; Escobedo, F. A. Simulation Study of Free-Energy Barriers in the Wetting Transition of an Oily Fluid on a Rough Surface with Reentrant Geometry. *Langmuir* **2012**, *28*, 16080–16090.
- (8) Sheng, Y.-J.; Jiang, S.; Tsao, H.-K. Effects of Geometrical Characteristics of Surface Roughness on Droplet Wetting. *J. Chem. Phys.* **2007**, *127*.
- (9) Henkelman, G.; Jonsson, H. Improved Tangent Estimate in the Nudged Elastic Band Method for Finding Minimum Energy Paths and Saddle Points. *J. Chem. Phys.* **2000**, *113*, 9978–9985.
- (10) Sheppard, D.; Terrell, R.; Henkelman, G. Optimization Methods for Finding Minimum Energy Paths. *J. Chem. Phys.* **2008**, *128*.
- (11) Granot, R.; Baer, R. A Spline for Your Saddle. *J. Chem. Phys.* **2008**, *128*.
- (12) Quapp, W. Chemical Reaction Paths and Calculus of Variations. *Theor. Chem. Acc.* **2008**, *121*, 227–237.
- (13) Li, Y.; Ren, W. Numerical Study of Vapor Condensation on Patterned Hydrophobic Surfaces Using the String Method. *Langmuir* **2014**, *30*, 9567–9576.
- (14) Kavousanakis, M. E.; Colosqui, C. E.; Papathanasiou, A. G. Engineering the Geometry of Stripe-Patterned Surfaces toward Efficient Wettability Switching. *Colloids Surf. A: Physicochem. Eng. Aspects* **2013**, *436*, 309–317.
- (15) E, W.; Ren, W. Q.; Vanden-Eijnden, E. String Method for the Study of Rare Events. *Phys. Rev. B* **2002**, *66*.
- (16) Henkelman, G.; Uberuaga, B. P.; Jonsson, H. A Climbing Image Nudged Elastic Band Method for Finding Saddle Points and Minimum Energy Paths. *J. Chem. Phys.* **2000**, *113*, 9901–9904.
- (17) Henkelman, G.; Jonsson, H. A Dimer Method for Finding Saddle Points on High Dimensional Potential Surfaces Using Only First Derivatives. *J. Chem. Phys.* **1999**, *111*, 7010–7022.
- (18) E, W.; Ren, W.; Vanden-Eijnden, E. Simplified and Improved String Method for Computing the Minimum Energy Paths in Barrier-Crossing Events. *J. Chem. Phys.* **2007**, *126*.
- (19) Qian, T. Z.; Wang, X. P.; Sheng, P. Molecular Scale Contact Line Hydrodynamics of Immiscible Flows. *Phys. Rev. E* **2003**, *68*.
- (20) Mickel, W.; Joly, L.; Biben, T. Transport, Phase Transitions, and Wetting in Micro/Nanochannels: A Phase Field/DDFT Approach. *J. Chem. Phys.* **2011**, *134*.
- (21) Kavousanakis, M. E.; Colosqui, C. E.; Kevrekidis, I. G.; Papathanasiou, A. G. Mechanisms of Wetting Transitions on Patterned Surfaces: Continuum and Mesoscopic Analysis. *Soft Matter* **2012**, *8*, 7928–7936.
- (22) Pooley, C. M.; Kusumaatmaja, H.; Yeomans, J. M. Contact Line Dynamics in Binary Lattice Boltzmann Simulations. *Phys. Rev. E* **2008**, *78*, 056709.
- (23) Vrancken, R. J.; Kusumaatmaja, H.; Hermans, K.; Prenen, A. M.; Pierre-Louis, O.; Bastiaansen, C. W. M.; Broer, D. J. Fully Reversible Transition from Wenzel to Cassie–Baxter States on Corrugated Superhydrophobic Surfaces. *Langmuir* **2010**, *26*, 3335–3341.
- (24) Osher, S.; Fedkiw, R. *Level Set Methods and Dynamic Implicit Surfaces*; Springer: 2003; Vol. 153.
- (25) Sethian, J. A.; Smereka, P. Level Set Methods for Fluid Interfaces. *Annu. Rev. Fluid Mech.* **2003**, *35*, 341–372.
- (26) De Menech, M. Modeling of Droplet Breakup in a Microfluidic T-Shaped Junction with a Phase-Field Model. *Phys. Rev. E* **2006**, *73*.
- (27) Jacqmin, D. Calculation of Two-Phase Navier–Stokes Flows Using Phase-Field Modeling. *J. Comput. Phys.* **1999**, *155*, 96–127.
- (28) Kim, J. Phase-Field Models for Multi-Component Fluid Flows. *Commun. Comput. Phys.* **2012**, *12*, 613–661.
- (29) Sun, Y.; Beckermann, C. Sharp Interface Tracking Using the Phase-Field Equation. *J. Comput. Phys.* **2007**, *220*, 626–653.
- (30) Backofen, R.; Voigt, A. A Phase-Field-Crystal Approach to Critical Nuclei. *J. Phys.: Condens. Matter* **2010**, *22*.
- (31) Ren, W. Wetting Transition on Patterned Surfaces: Transition States and Energy Barriers. *Langmuir* **2014**, *30*, 2879–2885.
- (32) Yue, P.; Zhou, C.; Feng, J. J. Spontaneous Shrinkage of Drops and Mass Conservation in Phase-Field Simulations. *J. Comput. Phys.* **2007**, *223*, 1–9.
- (33) Jacqmin, D. Contact-Line Dynamics of a Diffuse Fluid Interface. *J. Fluid Mech.* **2000**, *402*, 57–88.
- (34) Pashos, G.; Kokkoris, G.; Boudouvis, A. G. A Modified Phase-Field Method for the Investigation of Wetting Transitions of Droplets on Patterned Surfaces. *J. Comput. Phys.* **2015**, *283*, 258–270.
- (35) Kim, J.; Lee, S.; Choi, Y. A Conservative Allen–Cahn Equation with a Space-Time Dependent Lagrange Multiplier. *Int. J. Eng. Sci.* **2014**, *84*, 11–17.
- (36) Yue, P.; Zhou, C.; Feng, J. J.; Ollivier-Gooch, C. F.; Hu, H. H. Phase-Field Simulations of Interfacial Dynamics in Viscoelastic Fluids Using Finite Elements with Adaptive Meshing. *J. Comput. Phys.* **2006**, *219*, 47–67.
- (37) Yang, X.; Feng, J. J.; Liu, C.; Shen, J. Numerical Simulations of Jet Pinching-off and Drop Formation Using an Energetic Variational Phase-Field Method. *J. Comput. Phys.* **2006**, *218*, 417–428.
- (38) Yue, P. T.; Feng, J. J.; Liu, C.; Shen, J. A Diffuse-Interface Method for Simulating Two-Phase Flows of Complex Fluids. *J. Fluid Mech.* **2004**, *515*, 293–317.
- (39) Khatavkar, V. V.; Anderson, P. D.; Meijer, H. E. H. Capillary Spreading of a Droplet in the Partially Wetting Regime Using a Diffuse-Interface Model. *J. Fluid Mech.* **2007**, *572*, 367–387.
- (40) Yue, P.; Renardy, Y. Spontaneous Penetration of a Non-wetting Drop into an Exposed Pore. *Phys. Fluids* **2013**, *25*.
- (41) Xu, X.; Wang, X. Derivation of the Wenzel and Cassie Equations from a Phase Field Model for Two Phase Flow on Rough Surface. *SIAM J. Appl. Math.* **2010**, *70*, 2929–2941.
- (42) Lee, H. G.; Kim, J. Accurate Contact Angle Boundary Conditions for the Cahn–Hilliard Equations. *Comput. Fluids* **2011**, *44*, 178–186.
- (43) Khatavkar, V. V.; Anderson, P. D.; Duineveld, P. C.; Meijer, H. E. H. Diffuse-Interface Modelling of Droplet Impact. *J. Fluid Mech.* **2007**, *581*, 97–127.
- (44) Luo, K. F.; Kuittu, M. P.; Tong, C. H.; Majaniemi, S.; Alani-Nissila, T. Phase-Field Modeling of Wetting on Structured Surfaces. *J. Chem. Phys.* **2005**, *123*.
- (45) Vollmayr-Lee, B. P.; Rutenberg, A. D. Fast and Accurate Coarsening Simulation with an Unconditionally Stable Time Step. *Phys. Rev. E* **2003**, *68*.
- (46) Qiu, C.; Qian, T.; Ren, W. Application of the String Method to the Study of Critical Nuclei in Capillary Condensation. *J. Chem. Phys.* **2008**, *129*.
- (47) Zhu, J. Z.; Chen, L. Q.; Shen, J.; Tikare, V. Coarsening Kinetics from a Variable-Mobility Cahn–Hilliard Equation: Application of a Semi-Implicit Fourier Spectral Method. *Phys. Rev. E* **1999**, *60*, 3564–3572.
- (48) Vaikuntanathan, V.; Sivakumar, D. Transition from Cassie to Impaled State during Drop Impact on Groove-Textured Solid Surfaces. *Soft Matter* **2014**, *10*, 2991–3002.
- (49) Kannan, R.; Vaikuntanathan, V.; Sivakumar, D. Dynamic Contact Angle Beating from Drops Impacting onto Solid Surfaces Exhibiting Anisotropic Wetting. *Colloids Surf. A: Physicochem. Eng. Aspects* **2011**, *386*, 36–44.
- (50) Kannan, R.; Sivakumar, D. Drop Impact Process on a Hydrophobic Grooved Surface. *Colloids Surf. A: Physicochem. Eng. Aspects* **2008**, *317*, 694–704.
- (51) Guilizzoni, M.; Sotgia, G. Experimental Analysis on the Shape and Evaporation of Water Drops on High Effusivity, Microfinned Surfaces. *Exp. Therm. Fluid Sci.* **2010**, *34*, 93–103.
- (52) Jansen, H. P.; Sotthwes, K.; Ganser, C.; Teichert, C.; Zandvliet, H. J. W.; Kooij, E. S. Tuning Kinetics to Control Droplet Shapes on Chemically Striped Patterned Surfaces. *Langmuir* **2012**, *28*, 13137–13142.
- (53) Jansen, H. P.; Bliznyuk, O.; Kooij, E. S.; Poelsema, B.; Zandvliet, H. J. W. Simulating Anisotropic Droplet Shapes on Chemically Striped Patterned Surfaces. *Langmuir* **2012**, *28*, 499–505.
- (54) Papadopoulos, P.; Mammen, L.; Deng, X.; Vollmer, D.; Butt, H.-J. How Superhydrophobicity Breaks Down. *Proc. Natl. Acad. Sci. U.S.A.* **2013**, *110*, 3254–3258.

- (55) Patankar, N. A. Consolidation of Hydrophobic Transition Criteria by Using an Approximate Energy Minimization Approach. *Langmuir* **2010**, *26*, 8941–8945.
- (56) Paxson, A. T.; Varanasi, K. K. Self-Similarity of Contact Line Depinning from Textured Surfaces. *Nat. Commun.* **2013**, *4*.
- (57) Patankar, N. A. On the Modeling of Hydrophobic Contact Angles on Rough Surfaces. *Langmuir* **2003**, *19*, 1249–1253.
- (58) Giacomello, A.; Meloni, S.; Chinappi, M.; Casciola, C. M. Cassie–Baxter and Wenzel States on a Nanostructured Surface: Phase Diagram, Metastabilities, and Transition Mechanism by Atomistic Free Energy Calculations. *Langmuir* **2012**, *28*, 10764–10772.
- (59) Kavousanakis, M. E.; Russo, L.; Siettos, C. I.; Boudouvis, A. G.; Georgiou, G. C. A Timestepper Approach for the Systematic Bifurcation and Stability Analysis of Polymer Extrusion Dynamics. *J. Non-Newtonian Fluid Mech.* **2008**, *151*, 59–68.